2024 IEEE 18th International Conference on Control & Automation (ICCA)
June 18-21, 2024. Reykjavík, Iceland

First Principle Modeling of a Morphable Unmanned Aerial-Aquatic Vehicle: Mirs-Alioth

Dongyue Huang[1*], Minghao Dou[1*], Xuchen Liu[1], Ruixin Yan[1], Songqun Gao[1], Zixuan Liu[2], Biao Wang[3], Lihua Dou[4] and Ben M. Chen[1]

***Abstract*— This paper establishes a hybrid system model for a morphable unmanned aerial-aquatic vehicle (UAAV), named Mirs-Alioth, incorporating hydrodynamic parameters through the first principle. Unlike other current UAAVs, variable thrust tilt angles make Mirs-Alioth's model mutable. Thus, this paper directly employs geometric features of the vehicle, integrating a morphing model into a comprehensive dynamics of the vehicle and switching models between different media triggered by depth. The comprehensive model parameters including the rigid body part and the hydrodynamic part is then identified through experiments and computational fluid dynamic (CFD) methods.**

I. Introduction

In recent years, with the rapid development of the manufacturing industry, an increasing number of functional robots have gradually emerged in our field of vision. Common examples include ground robots (UGV), underwater robots (ROV/AUV), and aerial robots (UAV), among others. These robots have been developed to address various challenges encountered by humans in production and daily life, such as detection, search operations, and delivery services. As the development of robots in single media environments has matured over the years, attention has shifted towards cross-domain unmanned platforms as illustrated in [1], [2], termed as unmanned aerial-aquatic vehice (UAAV). Examples of such platforms include the Loon Copter in [3], the Nezha series platform in [4], [5], and the TJ-FlyingFish [6], [7]. Additionally, the coupling tiltable UAAVs developed by Tan [8] and Huang [9] are also part of this focus.

Modeling, a critical first step post-acquisition of the mechanical structure platform, has seen varying degrees of depth in previous morphable UAAV studies. For instance, Tan in [10] and Dou in [11] presented a basic model using Newton's Law for morphable UAAVs, yet it lacked a comprehensive treatment of time-varying hydrodynamics and morphing components. Drawing from other UAAV modeling efforts, the work done by Lu [12] on the Nezha III platform stands out for incorporating hydrodynamic parameters. However, the non-morphable nature of their platform significantly simplifies the dynamics. Neto's model [13] for his platform encountered similar limitations. Moreover, Bi [14] tackled the challenge of time-varying effects on stability by integrating a model with time-varying hydrodynamic parameters, albeit limited to cylindrical cabin shapes. Chen [15] offered a more comprehensive model, but the transition between media was simplified to linear density changes without thorough theoretical backing. Ravell [16] employed an automata for the hybrid system model, which, while innovative, risked chattering due to state jumps.

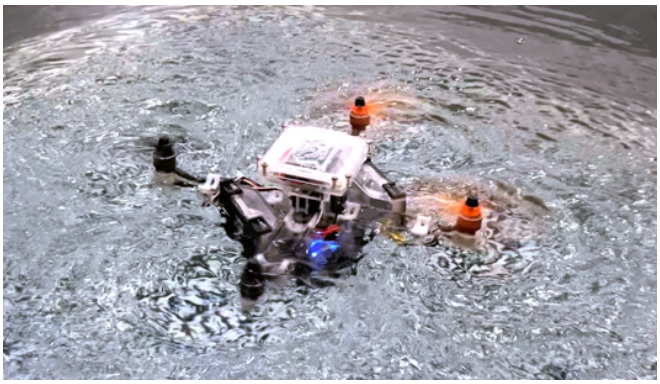

Fig. 1: Snapshot of Mirs-Alioth working during transition.

Addressing the challenges highlighted, this article focuses on a morphable UAAV prototype named Mirs-Alioth, developing a hybrid system model for it. Utilizing first principle, we individually establish the vehicle's model in air and underwater, with depth-driven switching between these states. To prevent chattering from frequent state changes, as seen with automata, we define safe switching zones for the model for smooth transitions. Moreover, we account for the hydrodynamics and the dynamic changes induced by morphing. Subsequent model parameter identification is conducted through experiments and Computational Fluid Dynamics (CFD). To this end, the main contributions of this note are summarized as follows,

1) Establish the vehicle's model for both aerial and aquatic environments using first principles and define safe switching zones to ensure smooth transitions between these states without chattering.
2) Incorporate the hydrodynamic part and the effects of morphing on rigid part into the model and validate these dynamic changes through experimental identification and CFD simulations.

The rest of the paper is organized as: Section II introduces

* denotes equal contribution.
[1]Department of Mechanical and Automation Engineering, The Chinese University of Hong Kong, Shatin, Hong Kong. {dyhuang,mhdou,xcliu,rxyan,sqgao,bmchen}@mae.cuhk.edu.hk
[2]Guangdong Laboratory of Artificial Intelligence and Digital Economy, Shenzhen, China. liuzixuan@gml.ac.cn
[3]College of Automation Engineering, Nanjing University of Aeronautics and Astronautics, Nanjing, Jiangsu, China. wangbiao@nuaa.edu.cn
[4]School of Automation, Beijing Institute of Technology, Beijing, China. doulihua@bit.edu.cn

2024 IEEE 18th International Conference on Control & Automation (ICCA) | 979-8-3503-5440-9/24/$31.00 ©2024 IEEE | DOI: 10.1109/ICCA62789.2024.10591869

the frame of reference and notations, which are used in the next modeling and disscusion. Section III gives a comprehensive model of the selected UAAV. After that, a detailed identification is given in Section IV based on the established model, including by using the method of experiments and CFD.

II. Frame of Reference and Notations

In this chapter, four reference frames are introduced: the body reference frame (b-frame), the inertial reference frame (e-frame), the base frame (base-frame), and the propulsion unit frame (p-frame), as shown in Fig. 2. On one hand, the b-frame's origin (O_b) is affixed to the center of gravity (CoG). On the other hand, the e-frame's origin (O_e) is affixed to the inertial plane in accordance with the North-East-Down (NED) convention. Additionally, the origin of a base coordinate system, denoted as O_base, is affixed at the centroid of the vehicle's lowest plane. Furthermore, the origin of p-frame is affixed to the centroid of the motor, denoted as O_p. Moreover, it should be noted that the vehicle exhibits symmetry along the x and y axis, but not along the z axis. Center of buoyancy (CoB) is the point at which the buoyant force acting on a submerged body is considered to be concentrated and the centroid of the vehicle according to Archimedes' principle.

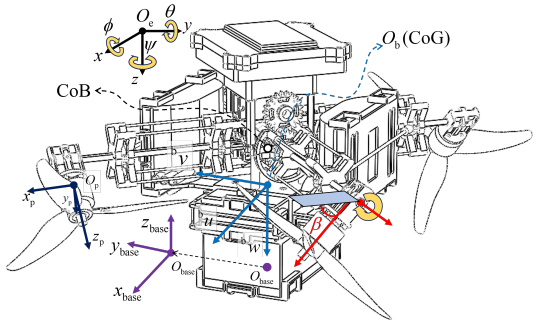

Fig. 2: Coordinates of Mirs-Alioth.

We define the state vector $\boldsymbol{\nu} = [{}^\mathrm{b}\boldsymbol{v}\ {}^\mathrm{b}\boldsymbol{\omega}]^\mathrm{T}$, encapsulating the vehicle's velocity within the body frame (b-frame), where ${}^\mathrm{b}\boldsymbol{v} = [u\ v\ w]^\mathrm{T}$ represents the body-fixed linear velocity and ${}^\mathrm{b}\boldsymbol{\omega} = [p\ q\ r]^\mathrm{T}$ denotes the body-fixed angular velocity. And the symmetrically thrust tilt angle denotes as β ranging from $-\pi/2$ to $\pi/2$ [8]. The pose variable $\boldsymbol{\eta} = [\boldsymbol{P}\ \boldsymbol{\Theta}]^\mathrm{T}$ comprises the position $\boldsymbol{P} = [x\ y\ z]^\mathrm{T}$ and the attitude represented by Euler angles $\boldsymbol{\Theta} = [\phi\ \theta\ \psi]^\mathrm{T}$, both expressed in the earth-fixed frame (e-frame). The transformation matrix $\boldsymbol{J} = \mathrm{diag}([\boldsymbol{R}_\mathrm{b}^\mathrm{e}, \boldsymbol{S}^{-1}])$ includes $\boldsymbol{R}_\mathrm{b}^\mathrm{e}$, the rotation matrix from the body frame to the earth frame, and $\boldsymbol{S}^{-1}$, the lumped transformation matrix for angular velocity, as detailed in [17], shown as

$$\boldsymbol{R}_\mathrm{b}^\mathrm{e} = \begin{bmatrix} c_\psi c_\theta & c_\psi c_\theta s_\phi - s_\psi c_\phi & s_\psi s_\phi + c_\psi c_\phi s_\theta \\ s_\psi c_\theta & s_\psi s_\theta s_\phi + c_\psi c_\phi & -c_\psi s_\phi + s_\psi c_\phi s_\theta \\ -s_\theta & c_\theta s_\phi & c_\theta c_\phi \end{bmatrix}, \tag{1}$$

$$\boldsymbol{S}^{-1} = \begin{bmatrix} 1 & s_\phi t_\theta & c_\phi t_\theta \\ 0 & c_\phi & -s_\phi \\ 0 & s_\phi / c_\theta & c_\phi / c_\theta \end{bmatrix}, \tag{2}$$

where $s(\cdot)$ denotes sin, $c(\cdot)$ denotes cos, $t(\cdot)$ denotes tan.

Additionally, the rotation matrix from the p-frame to the b-frame can be shwon as

$$\boldsymbol{R}_\mathrm{p}^\mathrm{b} = \frac{\sqrt{2}}{2} \begin{bmatrix} 1 & c_\beta - s_\beta & c_\beta \\ 1 & -s_\beta & c_\beta \\ 0 & \sqrt{2} c_\beta & -\sqrt{2} s_\beta \end{bmatrix}. \tag{3}$$

Additionally, the gravity and buoyancy forces acting on the vehicle are denoted by G and B, respectively. Other crucial parameters for the rigid body include the vehicle's mass m, the propulsion unit's mass (comprising the motor and propeller) m_p, and various distances measured relative to the vehicle's center of buoyancy (CoB), base (O_base), and body frame origin (O_b). These distances include Δz for the CoB to O_b, $z_\mathrm{b}(\beta)$ for CoB to O_base, and $z_\mathrm{g}(\beta)$ for O_b to O_base. Additionally, z_gp represents the distance from the propulsion unit's center of gravity (CoG) to its rotation axis, and z_gf denotes the distance from the fuselage's CoG to O_base. The parameters z_bp and z_bf indicate the distances from the propulsion unit's centroid and the fuselage's centroid to their rotation axis and O_base, respectively. The displacement volumes for the propulsion unit and fuselage are represented by V_p and V_f, while d_0 marks the distance between the propulsion unit's rotation axis and O_base. The distance from the force plane to the CoB is z_t, and the vehicle's moment of inertia is $\boldsymbol{I} = \mathrm{diag}([I_\mathrm{xx}, I_\mathrm{yy}, I_\mathrm{zz}])$. The moments of inertia for the propulsion unit and its base in the p-frame and b-frame are denoted as ${}^\mathrm{p}\boldsymbol{I}_\mathrm{p} = \mathrm{diag}([{}^\mathrm{p}I_\mathrm{xxp}, {}^\mathrm{p}I_\mathrm{yyp}, {}^\mathrm{p}I_\mathrm{zzp}])$ and ${}^\mathrm{b}\boldsymbol{I}_\mathrm{p} = \mathrm{diag}([{}^\mathrm{b}I_\mathrm{xxp}, {}^\mathrm{b}I_\mathrm{yyp}, {}^\mathrm{b}I_\mathrm{zzp}])$, respectively. The fuselage's moment of inertia is $\boldsymbol{I}_\mathrm{f} = \mathrm{diag}([I_\mathrm{xxf}, I_\mathrm{yyf}, I_\mathrm{zzf}])$, and the half wheelbase is indicated by l. Lastly, z_Δ specifies the maximum depth that ensures the propellers are exposed to the air.

In the context of hydrodynamics, the parameters related to added inertia resulting from acceleration, denoted as $X_\dot{\mathrm{u}}$, $Y_\dot{\mathrm{v}}$, $Z_\dot{\mathrm{w}}$, $K_\dot{\mathrm{p}}$, $M_\dot{\mathrm{q}}$, $N_\dot{\mathrm{r}}$, are of significant importance. Additionally, the damping coefficients, denoted as X_u, Y_v, Z_w, K_p, M_q, N_r, are also crucial hydrodynamic parameters.

Furthermore, we define $\boldsymbol{M}$ as the inertial matrix, $\boldsymbol{C}$ as the Coriolis/centripetal matrix, $\boldsymbol{D}$ as the damping matrix, $\boldsymbol{g}_{<k>}(\boldsymbol{\eta})$ as the generalized restoring force matrix. The vector of generalized force and moment is denoted as $\boldsymbol{\tau}_{<k>}$, and the input matrix is denoted as $\boldsymbol{B}_{<k>}(\beta)$, and the unestiblished model, and the external disturbance is denoted as $\boldsymbol{\tau}_\Delta$, and the input is denoted as $\boldsymbol{u}$ equaled to the square of the rotation speed of motors ϖ_i^2 ($i \in \{1, 2, 3, 4\}$). Moreover, the force/torque coefficients of the motor are denoted as $K_{<k>\mathrm{T}}$ and $K_{<k>\mathrm{M}}$. Besides, we also define the forces and moments in each axis as $[\boldsymbol{F_\mathrm{b}}\ \boldsymbol{T_\mathrm{b}}]^\mathrm{T} = [X\ Y\ Z\ K\ M\ N]^\mathrm{T}$, and the force and torque generalized by each actuator as f_i and τ_i. Here, the index of different medium denotes as k, shown as

$$< k > \in \{0 : \mathrm{air}, 1 : \mathrm{water}\}. \tag{4}$$

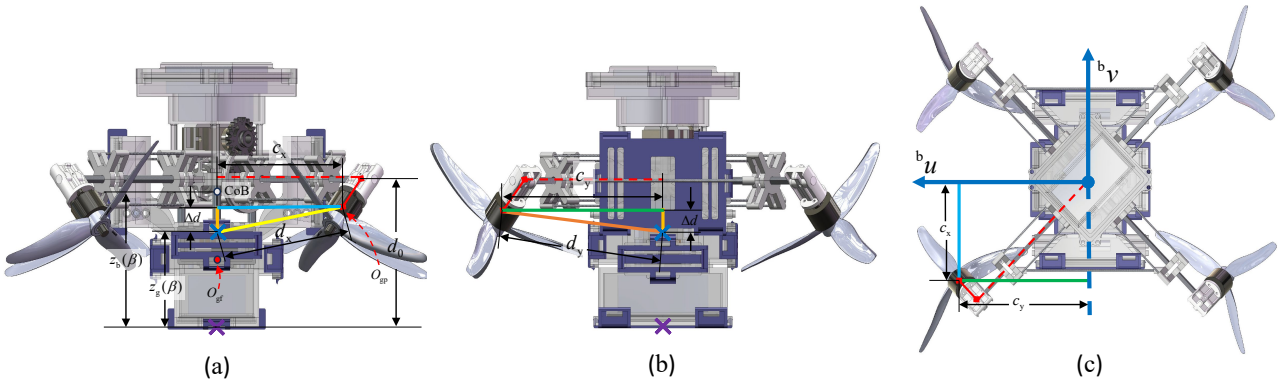

Fig. 3: Geometrical relations of Mirs-Alioth: (a) is the front view. (b) is the side view. (c) is the top view.

And e_* denotes the unit directional row vector for each state, where e_{z}, e_ϕ, e_θ and e_ψ are linearly independent, for example, $e_{\mathrm{z}} = [1\ 1\ 1\ 1]$, $e_\phi = e_{\mathrm{y}} = [-1\ 1\ 1\ -1]$, $e_\theta = -e_{\mathrm{x}} = [-1\ 1\ -1\ 1]$, and $e_\theta = [1\ 1\ -1\ -1]$.

III. Modeling

In this section, a comprehensive model for Mirs-Alioth under discrete events, like in aerial and underwater. Moreover, due to the servo actuation, the vehicle can alter the thrust direction, causing changes in the model due to morphability. However, given the relatively slow maximum underwater speed, we neglect the hydrodynamic effects caused by changes in the thrust direction in this modeling phase.

A. Comprehensive Model

The system model of Mirs-Alioth can be expressed in a general form that accommodates both aerial and aquatic modes, as shown in Fig. 4. Notably, medium-dependent changes only affect the dynamical model, whereas the kinematics model remains independent of such changes. And it can be represented as

$$\boldsymbol{M}\dot{\boldsymbol{\nu}} + \boldsymbol{C}\boldsymbol{\nu} + k \cdot \boldsymbol{D}\boldsymbol{\nu} + \boldsymbol{g}_{<k>}(\boldsymbol{\eta}) = \boldsymbol{\tau}_{<k>} + \boldsymbol{\tau}_\Delta, \tag{5}$$

$$\dot{\boldsymbol{\eta}} = \boldsymbol{J}\boldsymbol{\nu}, \tag{6}$$

with

$$\boldsymbol{M} = \boldsymbol{M}_{\mathrm{RB}} + k \cdot \boldsymbol{M}_{\mathrm{ADD}}, \tag{7}$$

$$\boldsymbol{C} = \boldsymbol{C}_{\mathrm{RB}} + k \cdot \boldsymbol{C}_{\mathrm{ADD}}, \tag{8}$$

$$\boldsymbol{\tau}_{<k>} = [\boldsymbol{F}_{\mathbf{b}}\ \boldsymbol{T}_{\mathbf{b}}]^{\mathrm{T}} = \boldsymbol{B}_{<k>}(\beta)\boldsymbol{u}. \tag{9}$$

To provide a more comprehensive understanding, we derive a generalized control effectiveness matrix (CEM) that is applicable to both aerial and aquatic modes, it yields at

$$\boldsymbol{B}_{<k>}(\beta) = \frac{\sqrt{2}}{2}\begin{bmatrix} c_\beta K_{<k>\mathrm{T}} \cdot e_{\mathrm{x}} \\ c_\beta K_{<k>\mathrm{T}} \cdot e_{\mathrm{y}} \\ -\sqrt{2} s_\beta K_{<k>\mathrm{T}} \cdot e_{\mathrm{z}} \\ k_{1<k>}(\beta) \cdot e_\phi \\ k_{2<k>}(\beta) \cdot e_\theta \\ \sqrt{2} k_{3<k>}(\beta) \cdot e_\psi \end{bmatrix}, \tag{10}$$

with

$$k_{1<k>}(\beta) = l \cdot s_\beta \cdot K_{<k>\mathrm{T}} + c_\beta(K_{<k>\mathrm{M}} - z_{\mathrm{t}} K_{<k>\mathrm{T}}), \tag{11}$$

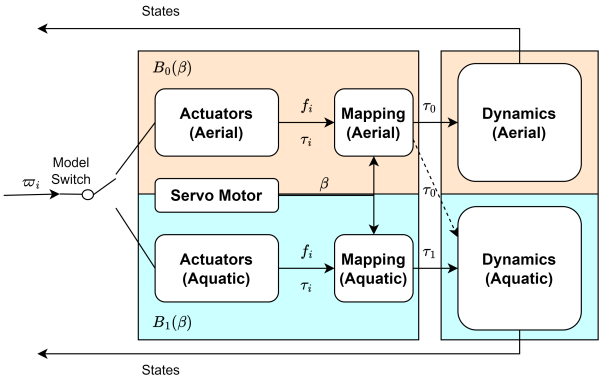

Fig. 4: Hybrid system model framework.

$$k_{2<k>}(\beta) = -l \cdot s_\beta \cdot K_{<k>\mathrm{T}} + c_\beta(K_{<k>\mathrm{M}} + z_{\mathrm{t}} K_{<k>\mathrm{T}}), \tag{12}$$

$$k_{3<k>}(\beta) = K_{<k>\mathrm{T}} l \cdot c_\beta - s_\beta \cdot K_{<k>\mathrm{M}}, \tag{13}$$

where $k_{i<k>}(\beta)$ is the coefficient of the body moment, and the force/torque coefficient of the motor denoted as $K_{<k>\mathrm{T}}$ and $K_{<k>\mathrm{M}}$.

Moreover, the generalized restoring force matrix can be organized as

$$\boldsymbol{g}_{<k>}(\boldsymbol{\eta}) = \begin{bmatrix} (G - k \cdot B)s_\theta \\ -(G - k \cdot B)c_\theta s_\phi \\ -(G - k \cdot B)c_\theta c_\phi \\ -\Delta z B \cdot c_\theta s_\phi \\ -\Delta z B \cdot s_\theta \\ 0 \end{bmatrix}. \tag{14}$$

Besides, the model switching logic is determined by depth event, detailed as

$$\begin{cases} z \geq 0, \ \text{Aquatic Mode}, & \text{(15a)} \\ z_\Delta > z \geq 0, \ \text{Aquatic Mode } (\boldsymbol{B}_0), & \text{(15b)} \\ z < 0, \ \text{Aerial Mode}. & \text{(15c)} \end{cases}$$

Undoubtedly, when the vehicle operates within a single medium, the model is either aerial or aquatic. However, during the transition from one medium to another, due to the propeller's position above the vehicle's origin, there is a phase where the propulsion unit's model remains aerial while

the body of the vehicle operates under aquatic conditions, which is the design principle illustrated in (15b).

B. Modeling of Morphing Part

Although we assume the hydrodynamic effects due to deformation are negligible, the changes in the rigid body model parameters caused by the vehicle's deformation cannot be overlooked. Specifically, the vehicle's center of gravity and buoyancy will vary with changes in the thrust tilt angle, and this relationship can be described as follows:

$$\Delta z(\beta) = z_{\mathrm{b}}(\beta) - z_{\mathrm{g}}(\beta), \tag{16}$$

$$z_{\mathrm{b}}(\beta) = \frac{4V_{\mathrm{p}}(z_{\mathrm{bp}}s_\beta + d_0) + V_{\mathrm{f}}z_{\mathrm{bf}}}{4V_{\mathrm{p}} + V_{\mathrm{f}}}, \tag{17}$$

$$z_{\mathrm{g}}(\beta) = \frac{4m_{\mathrm{p}}(z_{\mathrm{gp}}s_\beta + d_0) + (m - 4m_{\mathrm{p}})z_{\mathrm{gf}}}{m}. \tag{18}$$

As illustrated in Fig. 3, the geometry relations, influenced by varying thrust tilt angles, can be detailed as follows

$$d_{\mathrm{x}} = \sqrt{c_{\mathrm{x}}^2 + \Delta d^2}, \tag{19}$$

$$d_{\mathrm{y}} = \sqrt{c_{\mathrm{y}}^2 + \Delta d^2}, \tag{20}$$

$$d_{\mathrm{z}} = \sqrt{(z_{\mathrm{gp}}c_\beta)^2 + l^2}, \tag{21}$$

where

$$c_{\mathrm{x}} = \sin(\frac{\pi}{4} - \arctan(\frac{z_{\mathrm{gp}}c_\beta}{l}))d_{\mathrm{z}}, \tag{22}$$

$$c_{\mathrm{y}} = \cos(\frac{\pi}{4} - \arctan(\frac{z_{\mathrm{gp}}c_\beta}{l}))d_{\mathrm{z}}, \tag{23}$$

$$\Delta d = z_{\mathrm{gp}}s_\beta + d_0 - z_{\mathrm{g}}(\beta). \tag{24}$$

Furthermore, the moment of inertia experiences notable changes with adjustments in thrust tilt angles, and this relationship, along with the geometrical relations, can be elaborated on in detail,

$$\begin{aligned} I_{\mathrm{xx}} =& I_{\mathrm{xxf}} + (m - 4m_{\mathrm{p}})(z_{\mathrm{gf}} - z_{\mathrm{g}}(\beta))^2 \\ &+ 4({}^{\mathrm{b}}I_{\mathrm{xxp}} + m_{\mathrm{p}}d_{\mathrm{x}}^2), \end{aligned} \tag{25}$$

$$\begin{aligned} I_{\mathrm{yy}} =& I_{\mathrm{yyf}} + (m - 4m_{\mathrm{p}})(z_{\mathrm{gf}} - z_{\mathrm{g}}(\beta))^2 \\ &+ 4({}^{\mathrm{b}}I_{\mathrm{yyp}} + m_{\mathrm{p}}d_{\mathrm{y}}^2). \end{aligned} \tag{26}$$

$$I_{\mathrm{zz}} = I_{\mathrm{zzf}} + 4({}^{\mathrm{b}}I_{\mathrm{zzp}} + m_{\mathrm{p}}d_{\mathrm{z}}^2). \tag{27}$$

where

$${}^{\mathrm{b}}\boldsymbol{I}_{\mathrm{p}} = \boldsymbol{R}_{\mathrm{p}}^{\mathrm{b}} \cdot {}^{\mathrm{p}}\boldsymbol{I}_{\mathrm{p}} \cdot \boldsymbol{R}_{\mathrm{p}}^{\mathrm{b}\,\mathrm{T}}. \tag{28}$$

C. Modeling of Aerial Part

Due to the low viscosity of air, the damping terms caused by air resistance are often neglected. Substituting $k = 0$, the general dynamics model yields at

$$\boldsymbol{M}_{\mathrm{RB}}\dot{\boldsymbol{\nu}} + \boldsymbol{C}_{\mathrm{RB}}\boldsymbol{\nu} + \boldsymbol{g}_0(\boldsymbol{\eta}) = \boldsymbol{\tau}_0 + \boldsymbol{\tau}_\Delta. \tag{29}$$

We specify the thrust tilt angle to be fixed at $\pi/2$ in the aerial mode, because no morphing is considered in the aerial mode. And the inertial matrix shown in (29) is organized as

$$\boldsymbol{M}_{\mathrm{RB}} = \begin{bmatrix} m & 0 & 0 & 0 & m\Delta z & 0 \\ 0 & m & 0 & -m\Delta z & 0 & 0 \\ 0 & 0 & m & 0 & 0 & 0 \\ 0 & -m\Delta z & 0 & I_{\mathrm{xx}} & 0 & 0 \\ m\Delta z & 0 & 0 & 0 & I_{\mathrm{yy}} & 0 \\ 0 & 0 & 0 & 0 & 0 & I_{\mathrm{zz}} \end{bmatrix}. \tag{30}$$

Furthermore, the Coriolis/centripetal matrix in the air can also be represented as $\boldsymbol{C}_{\mathrm{RB}}$, and it can be shown in (31).

$$\boldsymbol{C}_{\mathrm{RB}}(\boldsymbol{\nu}) = \begin{bmatrix} 0 & 0 & 0 & m\Delta zr & mw & -mv \\ 0 & 0 & 0 & -mw & m\Delta zr & mu \\ 0 & 0 & 0 & m(\Delta zp - v) & m(\Delta zq + u) & 0 \\ -m\Delta zr & -mw & m(\Delta zp - v) & 0 & I_{\mathrm{zz}}r & -I_{\mathrm{yy}}q \\ -mw & -m\Delta zr & m(\Delta zq + u) & -I_{\mathrm{zz}}r & 0 & I_{\mathrm{xx}}p \\ mv & -mu & 0 & I_{\mathrm{yy}}q & -I_{\mathrm{xx}}p & 0 \end{bmatrix}. \tag{31}$$

D. Modeling of Aquatic Part

The general dynamics (5) can be transferred into dynamics for aquatic mode when $k = 1$, organized as

$$\boldsymbol{M}\dot{\boldsymbol{\nu}} + \boldsymbol{C}\boldsymbol{\nu} + \boldsymbol{D}\boldsymbol{\nu} + \boldsymbol{g}_1(\boldsymbol{\eta}) = \boldsymbol{\tau}_1 + \boldsymbol{\tau}_\Delta. \tag{32}$$

Unlike the modeling of the aerial part, the dynamics of the aquatic part should consider the hydrodynamic parameters owing to the high viscosity of water. Then the added mass matrix can be organized as

$$\boldsymbol{M}_{\mathrm{ADD}} = -\begin{bmatrix} X_{\dot{\mathrm{u}}} & 0 & 0 & 0 & Y_{\dot{\mathrm{p}}} & 0 \\ 0 & Y_{\dot{\mathrm{v}}} & 0 & X_{\dot{\mathrm{q}}} & 0 & 0 \\ 0 & 0 & Z_{\dot{\mathrm{w}}} & 0 & 0 & 0 \\ 0 & Y_{\dot{\mathrm{p}}} & 0 & K_{\dot{\mathrm{p}}} & 0 & 0 \\ X_{\dot{\mathrm{q}}} & 0 & 0 & 0 & M_{\dot{\mathrm{q}}} & 0 \\ 0 & 0 & 0 & 0 & 0 & N_{\dot{\mathrm{r}}} \end{bmatrix}. \tag{33}$$

Accordingly, the hydrodynamic Coriolis−Centripetal matrix generalized by the added mass matrix (33) can be derived as

$$\boldsymbol{C}_{\mathrm{ADD}}(\boldsymbol{\nu}) = \begin{bmatrix} 0 & 0 & 0 & 0 & -a_3 & a_2 \\ 0 & 0 & 0 & a_3 & 0 & -a_1 \\ 0 & 0 & 0 & -a_2 & a_1 & 0 \\ 0 & -a_3 & a_2 & 0 & -b_3 & b_2 \\ a_3 & 0 & -a_1 & b_3 & 0 & -b_1 \\ -a_2 & a_1 & 0 & -b_2 & b_1 & 0 \end{bmatrix}, \tag{34}$$

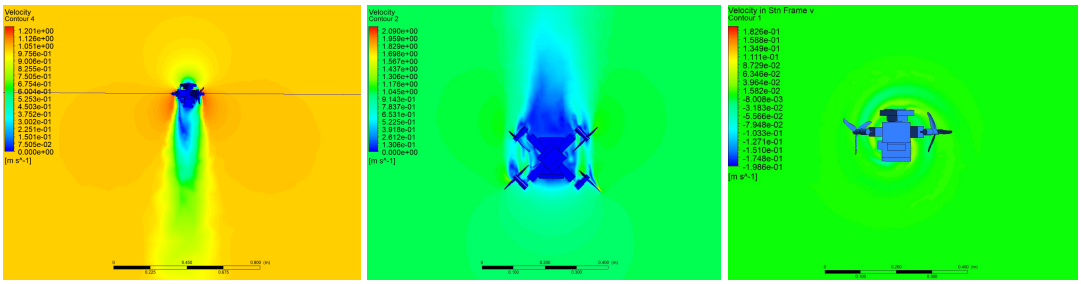

(a) (b) (c)

Fig. 5: Simulation results snapshot in CFD: (a) is the flow fluid test in the z-direction. (b) is the flow fluid test in the y-direction. (c) is the flow fluid test in the θ-direction.

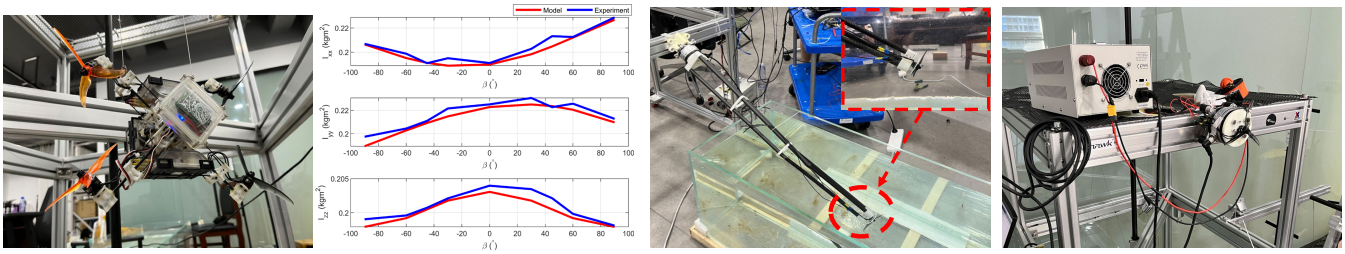

(a) (b) (c) (d)

Fig. 6: Experiment snapshots of Mirs-Alioth: (a) is the snapshot of hanging experience. (b) is the comparitive results of experiments and modeling. (c) and (d) are the snapshots of propulsion unit identification in aerial and aquatic.

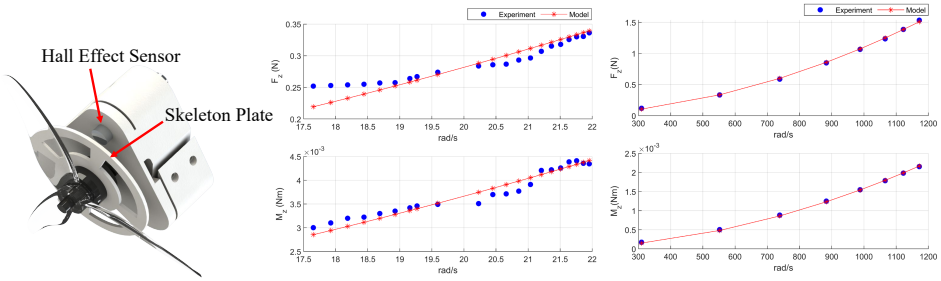

(a) (b) (c)

Fig. 7: (a) is the enlarged section of the identification setup of the aquatic propulsion unit. (b) is the result of identification and fitting model for the aquatic propulsion unit. (c) is the result of identification and the fitting model for the aerial propulsion unit.

with

$$\begin{cases} a_1 = X_{\dot{\mathrm{u}}} u + X_{\dot{\mathrm{q}}} q, \\ a_2 = Y_{\dot{\mathrm{v}}} v + Y_{\dot{\mathrm{p}}} p, \\ a_3 = Z_{\dot{\mathrm{w}}} w, \\ b_1 = K_{\dot{\mathrm{p}}} p + Y_{\dot{\mathrm{p}}} v, \\ b_2 = M_{\dot{\mathrm{q}}} q + X_{\dot{\mathrm{q}}} u, \\ b_3 = N_{\dot{\mathrm{r}}} r. \end{cases}$$

The damping term $\boldsymbol{D}$ neglecting the nonlinear damping is defined as:

$$\boldsymbol{D} = \mathrm{diag}([X_{\mathrm{u}}, Y_{\mathrm{v}}, Z_{\mathrm{w}}, K_{\mathrm{p}}, M_{\mathrm{q}}, N_{\mathrm{r}}]). \tag{36}$$

IV. System Identifications

In this section, we employ CFD simulations to derive the hydrodynamic parameters of the vehicle as depicted in Fig. 5. We set flow velocities in the x, y, and z directions to measure the corresponding forces, and in the ϕ, θ, and ψ directions to measure the torques, thereby determining the vehicle's damping parameters. Similarly, the added mass parameters are calculated as well.

For changes in rigid body dynamics caused by morphing, we use the commonly employed suspension method to measure alterations in the moment of inertia, as shown in part (a) of Fig. 6. Furthermore, as illustrated in part (b) of Fig. 6, a comparison between the theoretical moment of inertia model and experimental data validates our model, confirming its accuracy and reliability in representing the dynamics of morphing parts. Experimental identification of the propulsion unit's parameters is also conducted, as shown in parts (c) and (d) of Fig. 6. Due to high viscosity of water, the rotational speed of underwater motors is slow, which is

TABLE I: Model parameters of Mirs-Alioth

Attribute	Value
m (kg)	0.7
m_{p} (kg)	0.019
l (m)	0.125
d_0 (m)	0.082
z_{bf} (m)	0.0675
z_{bp} (m)	0.0232
z_{gf} (m)	0.0550
z_{gp} (m)	0.0264
z_{t} (m)	0.0525
B (N)	7.03
V_{p} (m^3)	9.493×10^{-6}
V_{f} (m^3)	6.650×10^{-4}
$\boldsymbol{I}_{\mathrm{f}}$ (kgm^2)	$\mathrm{diag}([0.122, 0.104, 0.072])$
${}^{\mathrm{p}}\boldsymbol{I}_{\mathrm{p}}$ (kgm^2)	$\mathrm{diag}([2.15, 2.15, 2.68])\times 10^{-4}$
$K_{0\mathrm{T}}$ ($\mathrm{Nrad}^{-2}\mathrm{s}^{-2}$)	1.0989×10^{-6}
$K_{0\mathrm{M}}$ ($\mathrm{Nmrad}^{-2}\mathrm{s}^{-2}$)	1.5789×10^{-9}
$K_{1\mathrm{T}}$ ($\mathrm{Nrad}^{-2}\mathrm{s}^{-2}$)	0.7041×10^{-3}
$K_{1\mathrm{M}}$ ($\mathrm{Nmrad}^{-2}\mathrm{s}^{-2}$)	0.9160×10^{-5}
X_{u} (kgs^{-1})	7.3339
Y_{v} (kgs^{-1})	9.7790
Z_{w} (kgs^{-1})	10.2610
K_{p} ($\mathrm{kgm}^2\mathrm{s}^{-1}$)	0.0037
M_{q} ($\mathrm{kgm}^2\mathrm{s}^{-1}$)	0.0040
N_{r} ($\mathrm{kgm}^2\mathrm{s}^{-1}$)	0.0127
$X_{\dot{\mathrm{u}}}$ (kg)	-0.5495
$X_{\dot{\mathrm{q}}}$ (kg)	3.76×10^{-3}
$Y_{\dot{\mathrm{p}}}$ (kg)	-4.53×10^{-3}
$Y_{\dot{\mathrm{v}}}$ (kg)	-0.6190
$Z_{\dot{\mathrm{w}}}$ (kg)	-0.4608
$K_{\dot{\mathrm{p}}}$ (kgm^2)	-0.0043
$M_{\dot{\mathrm{q}}}$ (kgm^2)	-0.0035
$N_{\dot{\mathrm{r}}}$ (kgm^2)	-0.0008

problematic for sensors that require speeds above 2000 rpm. As depicted in (a) of Fig. 7, which is the enlarged part of (c) Fig. 6, a skeleton plate is mounted on the motor, with a metal block attached to this plate. Each time the metal block passes the Hall effect sensor, the rotational speed data are recorded. This section also features a six-axis force/torque sensor to gather thrust and torque data. Part (d) illustrates the conventional aerial identification process, following standard procedures for air motor identification [18]. And as shown in (c) and (d) of Fig. 7, the established model can fit the identification result well. Therefore, the detailed parameters of the model are illustrated in Table I.

V. Conclusion

This paper has successfully developed the hybrid system model for the morphable UAAV, termed as Mirs-Alioth, by incorporating hydrodynamic parameters derived from first principle. In contrast to other UAAVs currently available, the adaptability of Mirs-Alioth's model is significantly enhanced due to the variable thrust tilt angles. This advancement has led the research to directly leverage the vehicle's geometric features, thereby integrating a dynamic morphing model into the vehicle's comprehensive dynamics framework. This integration facilitates seamless switching between models suited for different media, an action triggered by variations in depth. Through rigorous experimentation and the application of CFD methods, the detailed model has been thoroughly identified and characterized. While this paper has successfully established and validated the mathematical model for the Mirs-Alioth, some aspects are not considered, such as the hydrodynamic parameters influenced by morphing parts. These elements will be a primary focus in future research to enhance the accuracy of the model.

References

[1] Y. H. Tan and B. M. Chen, "Survey on the development of aerial-aquatic hybrid vehicles," *Unmanned Systems*, vol. 9, no. 3, pp. 263–282, 2021.

[2] Z. Zeng, C. Lyu, Y. Bi, Y. Jin, D. Lu, and L. Lian, "Review of hybrid aerial underwater vehicle: Cross-domain mobility and transitions control," *Ocean Engineering*, vol. 248, p. 110840, 2022.

[3] H. Alzu'bi, I. Mansour, and O. Rawashdeh, "Loon copter: Implementation of a hybrid unmanned aquatic–aerial quadcopter with active buoyancy control," *Journal of Field Robotics*, vol. 35, no. 5, pp. 764–778, 2018.

[4] Y. Bi, Y. Jin, C. Lyu, Z. Zeng, and L. Lian, "Nezha-mini: Design and locomotion of a miniature low-cost hybrid aerial underwater vehicle," *IEEE Robotics and Automation Letters*, vol. 7, no. 3, pp. 6669–6676, 2022.

[5] Y. Bai, Y. Jin, C. Liu, Z. Zeng, and L. Lian, "Nezha-f: Design and analysis of a foldable and self-deployable hauv," *IEEE Robotics and Automation Letters*, vol. 8, no. 4, pp. 2309–2316, 2023.

[6] X. Liu, M. Dou, D. Huang, B. Wang, J. Cui, Q. Ren, L. Dou, Z. Gao, J. Chen, and B. M. Chen, "Tj-flyingfish: Design and implementation of an aerial-aquatic quadrotor with tiltable propulsion units," in *2023 IEEE International Conference on Robotics and Automation (ICRA)*, 2023.

[7] X. Liu, M. Dou, R. Yan, D. Huang, S. Gao, B. Wang, J. Cui, Q. Ren, L. Dou, Z. Gao, J. Chen, and B. M. Chen, "Tj–flyingfish: An unmanned morphable aerial–aquatic vehicle system," *Unmanned Systems*, 2023.

[8] Y. H. Tan and B. M. Chen, "A morphable aerial-aquatic quadrotor with coupled symmetric thrust vectoring," in *2020 IEEE International Conference on Robotics and Automation (ICRA)*. IEEE, 2020, pp. 2223–2229.

[9] D. Huang, X. Liu, M. Dou, and B. M. Chen, "Systematizing rotor-based morphable unmanned aerial-aquatic vehicles design: From theory to prototype," in *OCEANS 2024 MTS/IEEE SINGAPORE*. IEEE, 2024, pp. 1–9.

[10] Y. H. Tan and B. M. Chen, "Underwater stability of a morphable aerial-aquatic quadrotor with variable thruster angles," in *2021 IEEE International Conference on Robotics and Automation (ICRA)*. IEEE, 2021, pp. 314–320.

[11] M. Dou, X. Liu, D. Huang, B. Wang, J. Cui, Q. Ren, L. Dou, J. Chen, and B. M. Chen, "Modeling and operating point analysis for aquatic translational motion of a cross-medium vehicle," in *Proceedings of the 42rd Chinese Control Conference*, 2023.

[12] D. Lu, C. Xiong, B. Lyu, Z. Zeng, and L. Lian, "Multi-mode hybrid aerial underwater vehicle with extended endurance," in *2018 OCEANS - MTS/IEEE Kobe Techno-Oceans (OTO)*, 2018, pp. 1–7.

[13] A. A. Neto, L. A. Mozelli, P. L. Drews, and M. F. Campos, "Attitude control for an hybrid unmanned aerial underwater vehicle: A robust switched strategy with global stability," in *2015 IEEE International Conference on Robotics and Automation (ICRA)*. IEEE, 2015, pp. 395–400.

[14] Y. Bi, D. Lu, Z. Zeng, and L. Lian, "Dynamics and control of hybrid aerial underwater vehicle subject to disturbances," *Ocean Engineering*, vol. 250, p. 110933, 2022.

[15] Y. Chen, Y. Liu, Y. Meng, S. Yu, and Y. Zhuang, "System modeling and simulation of an unmanned aerial underwater vehicle," *Journal of Marine Science and Engineering*, vol. 7, no. 12, p. 444, 2019.

[16] D. A. M. Ravell, M. M. Maia, and F. J. Diez, "Modeling and control of unmanned aerial/underwater vehicles using hybrid control," *Control Engineering Practice*, vol. 76, pp. 112–122, 2018.

[17] G. Cai, B. M. Chen, and T. H. Lee, *Unmanned rotorcraft systems*. Springer Science & Business Media, 2011.

[18] L. Wu, Y. Ke, and B. M. Chen, "Systematic modeling of rotor-driving dynamics for small unmanned aerial vehicles," *Unmanned Systems*, vol. 6, no. 02, pp. 81–93, 2018.